Attitude–Pattern Coupling: Antenna-Induced Non-Stationarity in Low-Altitude Air-to-Ground Channels

Rui Zhang, Zehong Lin, Mengyu Liang, Xiaoxin Yu, Yifan Gu, Suzhi Bi, Xiao Zhang, and Zhi Quan

***Abstract*—Unmanned aerial vehicle (UAV) air-to-ground (A2G) channels often exhibit intrinsic non-stationarity, which is commonly attributed to trajectory variations or scatterer evolution. However, existing studies largely overlook the interaction between UAV attitude dynamics and the non-uniform antenna radiation pattern. This paper reports a previously unrecognized stationarity-collapse phenomenon observed in low-altitude A2G measurements, where the channel stationarity time drops abruptly in the near-nadir region. To expose its physical origin, we design a lightweight wideband channel sounder with a pure-algorithm synchronization scheme, enabling high-fidelity measurements without heavy atomic-clock hardware. Measurement data reveal that when the line-of-sight (LoS) path intersects the steep gain gradient around the antenna's boresight null, micro-scale UAV wobbling is amplified into severe LoS power fluctuations, yielding rapid temporal non-stationarity. We formulate this mechanism as attitude–pattern coupling (APC) and develop an analytical model that integrates directional antenna characteristics with stochastic attitude dynamics. Specifically, closed-form expressions for the large-scale path loss and temporal autocorrelation function (ACF) are derived to theoretically quantify the channel instability. A new metric, the normalized dominant-path power (NDPP) distribution, is introduced to characterize the fluctuation depth. Comparative analysis involving analytical derivations, numerical simulations, and field experiments demonstrates a high degree of consistency. The results confirm that while attitude wobbling drastically expands the non-stationary zone near nadir, it induces negligible instability in low-elevation regions where the antenna gain is flat. The findings challenge the conventional distance-dependent stationarity assumption and provide fundamental insights for robust UAV communication system design in near-nadir operations.**

***Index Terms*—UAV communications, Air-to-Ground channel, non-stationarity, attitude-pattern coupling, antenna radiation pattern, channel measurement.**

I. Introduction

The burgeoning low-altitude economy, driven by the expanding applications of unmanned aerial vehicles (UAVs) in areas such as logistics, surveillance, and communication relaying, necessitates robust and efficient air-to-ground (A2G) wireless communication systems [1], [2]. This requires a profound understanding of the underlying propagation channel characteristics. Unlike traditional terrestrial channels, A2G channels exhibit unique features, among which non-stationarity emerges as a critical factor impacting system design and performance [3]. This non-stationarity, characterized by rapid temporal and spatial variations in channel statistics, invalidates the conventional wide-sense stationary uncorrelated scattering (WSSUS) assumption [4], [5]. Recent studies have further highlighted the complexity of these channels in diffuse multipath environments and ultra-wideband scenarios [6], necessitating advanced modeling and measurement approaches.

To address these complex dynamics, extensive theoretical research has been conducted on geometry-based stochastic models (GBSMs). Early models moved beyond simple linear trajectory assumptions to capture the highly dynamic nature of UAVs, incorporating arbitrary 3D trajectories [7] and realistic aeronautic mobility models [8]. Some works have specifically addressed low-altitude scenarios, such as the 3D non-stationary GBSM for UAV-to-ground vehicle-to-vehicle (V2V) channels [9]. Furthermore, sophisticated models have expanded to complex scenarios such as multi-UAV cooperative communications [10], air-to-air (A2A) links [11], and massive multiple-input multiple-output (MIMO) scenarios [12].

Notably, recent works have begun to consider the impact of UAV mechanical dynamics, such as rotation and wobbling, on channel non-stationarity [13]–[15]. For instance, [16] investigated the impact of rotary-wing UAV wobbling on mmWave channels, and [17] provided a fundamental analysis of wobbling-aware channel models. However, a critical gap remains regarding hovering or low-speed scenarios in the Sub-6 GHz band. In mmWave scenarios, due to the extremely short wavelength, millimeter-level displacements induced by wind or mechanical vibration are sufficient to trigger significant micro-Doppler effects and phase noise [16]. Consequently, existing models typically treat attitude variations solely as geometric coordinate transformations affecting the phase or Doppler shifts, often under the assumption of isotropic antennas. In contrast, at lower frequency bands like Sub-6 GHz, the decimeter-level wavelength renders the micro-Doppler effect of such small displacements negligible. While these models acknowledge that antenna position changes affect non-stationarity [18], they generally overlook the critical interaction between the UAV's dynamic attitude and the non-

This work was supported in part by the National Natural Science Foundation of China under Grant No. 62471311 and No. 62271325, and in part by the Guangdong Basic and Applied Basic Research Foundation under Project 2024B1515020089, and in part by Shenzhen Science and Technology Program under Project JCYJ20250604181912016. *(Corresponding author: Zhi Quan.)*

The authors are with the State Key Laboratory of Radio Frequency Heterogeneous Integration, Guangdong Provincial Key Laboratory of Intelligent Information Processing, and College of Electronics and Information Engineering, Shenzhen University, Shenzhen 518060, China (e-mail: zhrrygh@szu.edu.cn; 2410044084@mails.szu.edu.cn; szu_lmy@163.com; yuxiaoxin2002@126.com; yifan.gu@szu.edu.cn; bsz@szu.edu.cn; xiao.zhang@szu.edu.cn; zquan@szu.edu.cn).

uniform radiation pattern of practical antennas—an amplitude modulation mechanism that fundamentally differs from phase-domain disturbances.

Parallel to theoretical modeling, field measurement campaigns are essential for validating channel characteristics. Unlike traditional channel sounders that maintain clock alignment via wired connections [19], the UAV-aided A2G scenario inherently necessitates a physically separated transceiver architecture. A critical challenge in A2G measurements is maintaining precise synchronization between physically separated transceivers. Foundational campaigns typically relied on high-end hardware solutions, such as GPS-disciplined oscillators (GPSDOs) or Rubidium atomic clocks, to ensure frequency and time stability [20], [21]. Even in recent advanced measurements for massive MIMO [12], reliance on heavy synchronization hardware remains common. Other approaches utilize complex two-way wireless handshake protocols to achieve synchronization [22], or rely on commercial network signals (e.g., LTE) which impose limitations on the sounding signal design [23], [24].

Despite these advancements, current research faces a dual dilemma. **On the modeling front**, existing works typically attribute the non-stationarity induced by UAV wobbling to the geometric displacement of the transceiver, which primarily drives phase-domain variations [15]–[17]. While this geometric perspective is fundamental, it often overlooks the impact of the antenna's non-uniform radiation pattern. Our work complements this view by identifying the coupling between attitude dynamics and spatial gain gradients as a critical driver of instability. Specifically, when micro-scale wobbling aligns with steep gain transitions (e.g., boresight nulls), it triggers severe amplitude fluctuations and "stationarity collapse" that displacement-based models alone cannot fully explain. **On the system design front**, existing measurement solutions suffer from significant trade-offs: hardware-based synchronization (e.g., atomic clocks) is often too heavy for small UAVs [25], while protocol-based schemes lack the flexibility required for custom channel sounding.

To bridge these gaps, this paper presents a comprehensive study encompassing system design, theoretical modeling, and experimental validation. The major contributions are summarized as follows:

- **Theoretical Derivation of APC Dynamics:** We explicitly incorporate the antenna's non-uniform radiation pattern—modeled via Bessel functions—into the non-stationary channel modeling framework. By applying first-order Taylor expansions to the attitude dynamics, we derive closed-form expressions for the time-varying path loss and the temporal autocorrelation function (ACF). These derivations mathematically characterize how the antenna gain gradient modulates the line-of-sight (LoS) coherence.
- **Lightweight System Design with Algorithmic Synchronization:** We developed a split-type A2G channel sounder that eliminates the need for heavy atomic clocks or complex hardware links. Instead, we propose a novel pure-algorithm synchronization scheme. By exploiting the deterministic presence of the LoS path in A2G environments, we accurately estimate the sampling time offset (STO) drift and align the LoS components across the burst, achieving high-fidelity synchronization using cost-effective hardware.
- **Verification of Attitude-Pattern Coupling (APC) Effect:** We identify and verify the APC mechanism through a triangulation of analytical derivation, numerical simulation, and extensive field measurements. The comparison results demonstrate distinct consistency between the theoretical ACF and empirical data, confirming that when the unavoidable mechanical wobbling of the UAV couples with the antenna's gain null, it triggers a "stationarity collapse" in specific spatial regions.

II. APC Channel Model

Existing GBSMs effectively capture non-stationarity arising from large-scale trajectory changes or scatterer evolution. However, they typically simplify the antenna radiation pattern as a static gain factor. It is crucial to recognize that investigating the antenna's spatially non-uniform gain gradient is not merely a specific case study but a fundamental necessity for A2G channel modeling. Unlike terrestrial networks, A2G links operate in a 3D space where the communication link inevitably sweeps through a wide elevation range.

TABLE I
DEFINITION OF SIGNIFICANT PARAMETERS.

Parameter	Definition	Unit
$\mathcal{A}(\theta)$	Normalized amplitude radiation pattern	Dimensionless
$\mathcal{A}_{GS}(\cdot)$	Antenna radiation pattern of the GS	Dimensionless
$\mathcal{A}_{UAV}(\cdot)$	Antenna radiation pattern of the UAV	Dimensionless
$\mathcal{A}'_{UAV}(\cdot)$	First-order derivative of the UAV antenna pattern	$1/\text{rad}$
$\theta_a(t), \theta_g(t)$	Static off-boresight angle and geometric elevation angle	rad
η_n	Power allocation factor of the n-th NLoS path	Dimensionless
$\psi(t)$	Instantaneous attitude deviation (wobbling angle)	rad
$K(t)$	Rician K-factor (relative power ratio)	Dimensionless
$\Omega(t)$	Time-varying average channel gain	Dimensionless
$G_p[i], \overline{G_p}[s]$	Instantaneous channel power gain and large-scale average power gain	Dimensionless
$\overline{PL}[s]$	Large-scale path loss for the s-th measurement burst	dB

In this work, we focus on the near-nadir region as a representative scenario to expose this effect. As shown in the anechoic chamber measurements of radiation pattern in Fig. 1, the custom circular patch antenna employed in our study is characterized by a boresight null (due to its higher-order mode design), which creates an exceptionally steep gain gradient—measured at up to 6 dB/deg. This specific hardware characteristic provides an ideal physical environment to isolate and observe the interaction between the antenna's anisotropic gain and the UAV's instantaneous attitude variations. We find that the coupling between this steep gradient and micro-scale mechanical wobbling triggers a stationarity collapse that existing models overlook.

To theoretically characterize this mechanism, we propose a novel APC channel model. By explicitly integrating these

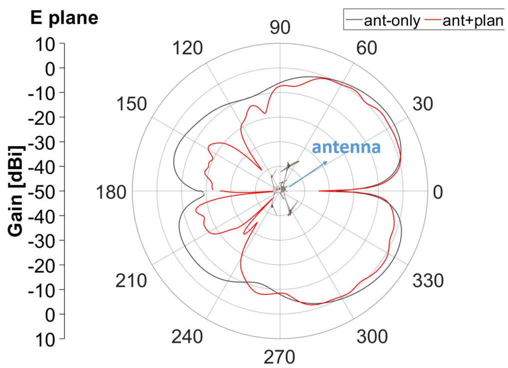

(a) Polar plot comparing standalone vs. mounted patterns, revealing ripples induced by airframe blockage.

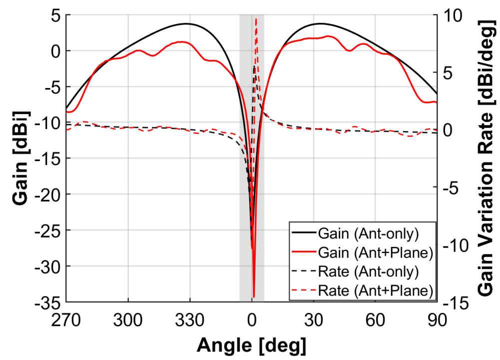

(b) Cartesian analysis of gain and its variation rate. The gray shaded area identifies the antenna-induced attenuation region (AIAR) near the nadir ($0°$), where the steep gain gradient causes high sensitivity to attitude wobbling.

Fig. 1. Measured elevation radiation characteristics of the custom patch antenna used in this study. The steep gradient near the nadir motivates the proposed APC model.

measured high-gradient characteristics with stochastic attitude dynamics, this framework provides a generalizable physical basis for analyzing channel instability in any region with rapid gain transitions.

A. General Channel Framework

Consider an A2G communication link where a UAV acts as the transmitter (TX) to transmit signals to a ground station (GS). The channel impulse response (CIR) can be modeled as a superposition of a deterministic LoS component and stochastic non-line-of-sight (NLoS) multipath components. In typical A2G communication scenarios, influenced by factors such as UAV movement, attitude variations, dynamic blockage, and differences in the scattering environment of the flight area, the relative power ratio between the LoS and NLoS components (i.e., the Rician K-factor) varies significantly over time [26]. Consequently, the channel amplitude follows a Rician distribution with a time-varying K-factor $K(t)$. The complex baseband CIR can be expressed as

$$h(t,\tau) = \sqrt{\frac{\Omega(t)K(t)}{K(t)+1}} h_{\mathrm{LoS}}(t,\tau) + \sqrt{\frac{\Omega(t)}{K(t)+1}} h_{\mathrm{NLoS}}(t,\tau), \tag{1}$$

where t represents the observation time and τ denotes the propagation delay. The parameter $\Omega(t)$ is defined as the time-varying average channel gain, whose value is primarily determined by large-scale path loss and depends solely on the propagation environment, excluding the directional gains provided by the transmitting and receiving antennas. Given that the LoS path accounts for the vast majority of the energy in typical scenarios, we focus on characterizing the dynamic properties of $h_{\mathrm{LoS}}(t,\tau)$.

B. Analytical Antenna Pattern Modeling

To mathematically characterize the impact of the antenna, we model the radiation pattern as a function of the off-boresight angle θ relative to the nadir. To ensure consistency with the geometric coordinate transformations derived later, we define θ over the full angular period $[0, 2\pi)$. However, given the operational scenario where the UAV maintains a higher altitude than the GS and the antenna is mounted facing downwards, the effective signal propagation is physically confined to the lower hemisphere (i.e., the sector spanning $270° \to 0° \to 90°$). We model the normalized amplitude radiation pattern, $\mathcal{A}(\theta)$, using the first-order Bessel function of the first kind, $J_1(\cdot)$, modified to account for practical hardware imperfections [27], as

$$\mathcal{A}(\theta) = \frac{J_1(\beta\,|\sin\theta|) + \epsilon}{J_{1,\mathrm{peak}} + \epsilon}, \quad \theta \in [-\frac{\pi}{2}, \frac{\pi}{2}], \tag{2}$$

where ϵ represents the finite null depth factor, introduced to model the residual gain observed at the theoretical null as shown in Fig. 1 due to airframe blockage and cross-polarization. $J_{1,\mathrm{peak}} \approx 0.5819$ corresponds to the global maximum of the Bessel function, making $J_{1,\mathrm{peak}} + \epsilon$ the normalization constant ensuring $\max(\mathcal{A}(\theta)) = 1$. The beamwidth parameter β is calibrated by aligning the theoretical peak argument around 1.841 with the measured angle of maximum gain ($\theta_{\max} = 38°$ for our antenna), satisfying $\beta \sin(\theta_{\max}) = 1.841$.

The resulting simulated radiation pattern is visualized in Fig. 2. The solid curve represents the normalized gain, which faithfully reproduces the attenuation characteristic observed in the measurements. The dashed line illustrates the "gain variation rate" (derivative), highlighting that the gain gradient is maximized in the vicinity of the null. This steep slope is the root cause of the high sensitivity to attitude variations.

C. Attitude-Pattern Coupled LoS Component

The modeling of the LoS component is the core contribution of the APC model, defining the coupling mechanism between the geometric trajectory and stochastic attitude dynamics. The proposed LoS channel coefficient is modeled as

$$h_{\mathrm{LoS}}(t,\tau) = \mathcal{A}_{\mathrm{GS}}(\theta_a(t))\, \mathcal{A}_{\mathrm{UAV}}(\theta_a(t)+\psi(t)) \cdot e^{j[2\pi f_{\mathrm{d},0}(t)t - 2\pi f_c \tau_0(t)]}\, \delta(\tau - \tau_0(t)), \tag{3}$$

where $f_{\mathrm{d},0}(t)$ denotes the Doppler frequency shift of the LoS path, f_c denotes the carrier frequency and $\tau_0(t)$ represents the instantaneous propagation delay of the LoS path.

In (3), $\mathcal{A}_{\mathrm{GS}}(\cdot)$ represents the antenna radiation pattern of the GS. Since the GS antenna is mounted vertically facing

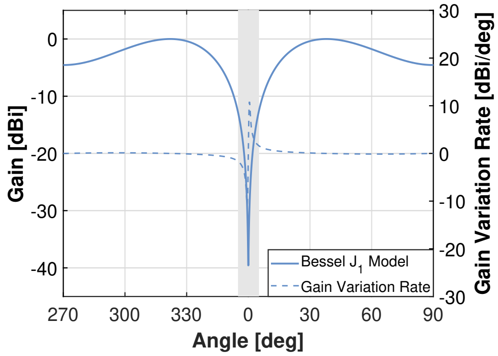

Fig. 2. Simulated antenna radiation pattern based on the modified Bessel J_1 model.

the zenith, its gain is characterized by the off-boresight angle $\theta_a(t)$ (the angle between the LoS path and the UAV antenna's boresight). The relationship between $\theta_a(t)$ and the geometric elevation angle $\theta_{\rm g}(t)$ is given by

$$\theta_a(t) = \left[\frac{\pi}{2} - \theta_{\rm g}(t)\right] \bmod 2\pi, \tag{4}$$

where the operator $[\cdot] \bmod 2\pi$ maps the argument into the interval $[0, 2\pi)$. Let $p_{\rm GS} = [0,0,0]^{\rm T}$ and $p_{\rm UAV}(t) = [x(t), y(t), z(t)]^{\rm T}$ denote the Cartesian coordinates of the GS and UAV, respectively. The geometric elevation angle is derived as

$$\theta_{\rm g}(t) = \arctan\left(\frac{z(t)}{\sqrt{x(t)^2 + y(t)^2}}\right). \tag{5}$$

In parallel, $\mathcal{A}_{\rm UAV}(\cdot)$ characterizes the radiation pattern of the UAV antenna. In contrast to the zenith-facing GS antenna, the UAV antenna is mounted in a downward-looking configuration (facing the nadir). While it shares the same underlying geometric LoS with the GS, its effective instantaneous angle of departure is further perturbed by the UAV's physical state. In realistic flight conditions, the UAV experiences unavoidable mechanical wobbling due to rotor vibration and wind resistance. We model this instantaneous attitude deviation (wobbling angle) $\psi(t)$ as a periodic process that reflects the rhythmic nature of mechanical resonance, expressed as

$$\psi(t) = \psi_{\max} \sin(2\pi f_w t + \phi_0), \tag{6}$$

where $\psi_{\max}$ is the maximum wobbling amplitude, f_w is the wobbling frequency, and ϕ_0 is a random initial phase. Consequently, the effective angle for the UAV antenna becomes the superposition of the static geometric angle and the dynamic wobbling: $\theta_{\rm UAV}(t) = \theta_a(t) + \psi(t)$.

To further reveal the relationship between attitude jitter and LoS power fluctuations, a first-order Taylor expansion is performed on the UAV antenna gain term at the static off-boresight angle $\theta_a(t)$, yielding

$$\mathcal{A}_{\rm UAV}(\theta_a(t) + \psi(t)) \approx \mathcal{A}_{\rm UAV}(\theta_a(t)) + \mathcal{A}'_{\rm UAV}(\theta_a(t))\psi(t), \tag{7}$$

where $\mathcal{A}'(\cdot)$ denotes the first-order derivative (or gain gradient) of the antenna radiation pattern with respect to the off-boresight angle θ. Considering the axial symmetry of the antenna pattern, we derive the sensitivity factor $\mathcal{A}'_{\rm UAV}(\theta_a(t))$ for the positive angular domain ($\theta \in [0, \frac{\pi}{2}]$). By applying the chain rule to the radiation pattern model, the gradient is given by

$$\begin{aligned}\mathcal{A}'_{\rm UAV}(\theta_a(t)) = &\frac{\beta \cos\theta_a(t)}{J_{1,\rm peak} + \epsilon} \\ &\cdot \left[J_0(\beta \sin\theta_a(t)) - \frac{J_1(\beta\sin\theta_a(t))}{\beta \sin\theta_a(t)}\right],\end{aligned} \tag{8}$$

where $J_0(\cdot)$ denotes the zeroth-order Bessel function of the first kind.

As shown in Fig. 2, when the UAV is at a high elevation angle ($\theta_{\rm g}(t) \approx \pi/2$), it enters the antenna-induced attenuation region (AIAR) where the off-boresight angle $\theta_a(t) \approx 0$. In this region, the gradient term $\mathcal{A}'_{\rm UAV}$ is maximized, amplifying small variations in $\psi(t)$ into large fluctuations in channel amplitude. Conversely, in the low-elevation region where the off-boresight angle corresponds to the main lobe, the gain curve is flat ($\mathcal{A}'_{\rm UAV} \approx 0$), rendering the impact of $\psi(t)$ negligible.

D. NLoS Component

In contrast to the LoS path, the NLoS components are largely insensitive to micro-scale attitude wobbling $\psi(t)$. This insensitivity arises because NLoS paths typically originate from prominent scatterers located at relatively large off-boresight angles, falling within the broad main lobe where the radiation pattern is approximately flat ($\mathcal{A}'_{\rm UAV} \approx 0$). Consequently, the effective antenna gain $\mathcal{A}_n$ for each NLoS path remains effectively constant. To isolate the rapid LoS power fluctuations induced by the APC effect, we assume the far-field scattering environment is quasi-static over short observation intervals. By abstracting away macro-scale scatterer evolution (such as the birth-death processes common in high-mobility models), we adopt the classical independent Sum-of-Sinusoids (SoS) approach to model the NLoS component, expressed as

$$\begin{aligned}h_{\rm NLoS}(t,\tau) = &\sum_{n=1}^{N_{\rm cl}} \eta_n \mathcal{A}_n e^{j(2\pi f_{{\rm d},n}(t)t + \phi_n - 2\pi f_c \tau_n(t))} \\ &\cdot \delta(\tau - \tau_n(t)),\end{aligned} \tag{9}$$

where $N_{\rm cl}$ denotes the total number of multipath components, η_n represents the power allocation factor of the n-th path with $\sum_{n=1}^{N_{\rm cl}} \eta_n = 1$. ϕ_n denotes the random phase offset of the n-th NLoS path induced by reflection interactions and is assumed to follow a uniform distribution over $[0, 2\pi)$, while $f_{{\rm d},n}(t)$ and $\tau_n(t)$ denote the instantaneous Doppler shift and propagation delay of the n-th path, respectively. This decoupled characterization of LoS and NLoS dynamics enables a clear isolation and analysis of the specific impact of attitude jitter on the dominant LoS path.

III. UAV-AIDED A2G CHANNEL SOUNDER

To experimentally validate the APC model proposed in Section II and investigate the non-stationary characteristics of real-world A2G channels, we designed a lightweight, split-type channel measurement system. As illustrated in Fig. 3, the system comprises an airborne TX and a ground-based receiver

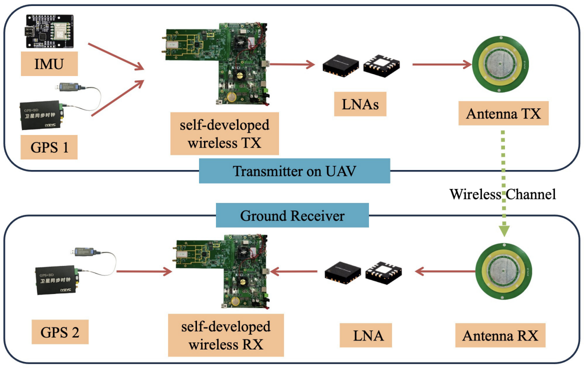

Fig. 3. System architecture of the UAV-aided channel sounder.

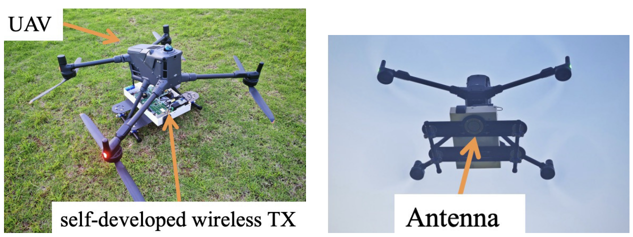

(a) Integration of the custom transceiver, IMU, and GPS on the UAV platform.

(b) Underside view showing the nadir-pointing antenna configuration.

Fig. 4. Hardware implementation of the airborne transmitter.

(RX). Instead of relying on heavy hardware synchronization solutions (e.g., Rubidium clocks), our system is built upon a custom-developed FPGA-based wireless architecture, tailored to support the algorithmic synchronization scheme detailed in Section IV.

A. Hardware Configuration

The physical implementation of the TX is shown in Fig. 4. The system is mounted on a commercial quadrotor UAV, ensuring a stable aerial platform. The core communication module is a custom-developed wideband transceiver integrating an FPGA for baseband processing and a high-performance RF frontend. The system operates in the 3.0–3.1 GHz band. To correlate channel data with flight dynamics, the TX integrates the GPS and the inertial measurement unit (IMU) modules. Detailed specifications are summarized in Table II. The RX system adopts a symmetric hardware architecture to the TX, utilizing an identical transceiver and GPS module to establish the ground reference.

Both the TX and RX employ custom-designed circular patch antennas to ensure omnidirectional coverage in the azimuth plane. On the TX side, the antenna is mounted on the underside of the airframe facing the nadir, as shown in Fig. 4b. As detailed in Section II, these antennas exhibit a distinct gain null at the boresight and a high gain variation rate in the near-nadir region. This measured characteristic serves as the physical basis for the stationarity collapse phenomenon analyzed in this paper. Specifically, the steep slope of the gain curve in the AIAR implies that even minute angular deviations (wobbling) will induce significant gain fluctuations.

TABLE II
EXPERIMENTAL HARDWARE PLATFORM SPECIFICATIONS

Component	Features
UAV	- Max. Payload: 6 kg - Max. Horiz. Speed: 25 m/s - Max. Takeoff Alt.: 7000 m
Wireless transceiver	- Freq. Range: 300 MHz – 6 GHz - Bandwidth: up to 100 MHz - Sampling Rate: 100 Msps
GPS module	- L1 Band (1575.42 MHz) - Position Update Rate: 1 Hz - 1-PPS Accuracy: $<$ 10 ns
IMU	- 10-axis - Update Rate: 60 Hz
LNA	- Freq. Range: 400 MHz – 8 GHz - Gain: approx. 23 dB
Antenna	- Azimuth: Omnidirectional - Elevation Max Gain: @ 38 deg - Peak Gain: 3.58 dBi

The measurement campaign employs a trigger-based synchronization scheme to coordinate the spatially separated TX and RX. The high-precision 1-PPS signal generated by the GPS modules serves as the global timing reference. On the rising edge of the PPS pulse, the TX initiates the transmission of the sounding signal burst, while the RX synchronously begins data capture. This mechanism establishes a coarse alignment for each measurement cycle. Due to hardware latencies and GPS jitter, a residual timing offset (approximately ± 40 ns) remains, which is addressed by the algorithmic synchronization described in Section IV. The system operates with a periodicity of 1 second. Within each cycle, the signal burst lasts for approximately 40 ms. Crucially, the data recording of the IMU is also triggered by the same PPS signal, ensuring strict temporal alignment between the captured CIRs and the UAV's attitude dynamics. Finally, the raw data from both the transceiver, the GPS, and the IMU are stored locally for offline processing.

B. Sounding Signal

To accurately estimate the time-varying CIR under a full operating bandwidth of 100 MHz, we employ the Zadoff-Chu (ZC) sequence $x[n]$, where the sequence length is $N_{\text{ZC}} = 1023$ and the root index $u = 1$, due to its ideal periodic auto-correlation and constant-amplitude zero auto-correlation properties. We designed a specific frame structure to support robust channel estimation in dynamic conditions. Each frame consists of two distinct parts:

1) Active Signal Part: This comprises two consecutive, identical ZC sequences ($T_{\text{act}} \approx 20.46$ μs). This dual-sequence design serves two critical purposes: it allows for coherent averaging to enhance the signal-to-noise ratio (SNR), and improves synchronization robustness by enabling the rejection of spurious correlation peaks that lack the expected N_{ZC}-sample interval.

2) Guard Interval (GI): A zero-padded interval with a duration of $T_{\text{GI}} \approx 30$ μs follows the active signal. This duration is selected to be significantly longer than the maximum expected delay spread of the A2G channel, effectively preventing inter-symbol interference (ISI) caused by multipath propagation. Consequently, the total frame duration is $T_{\text{period}} \approx 50\ \mu$s. Triggered by the PPS signal, the TX emits a burst of 800 frames (approximately 40 ms) every second. This configuration yields a high snapshot rate, providing the fine temporal resolution necessary for the algorithmic synchronization discussed in Section IV.

IV. Data Preprocessing

The proposed lightweight A2G system necessitates a physically separated transceiver architecture, which inevitably introduces hardware-induced impairments—primarily STO—originating from independent local oscillators. Distinct from conventional solutions that address these challenges using additional hardware references (e.g., bulky Rubidium atomic clocks) or complex synchronization protocols, we propose a novel *pure-algorithmic* synchronization framework leveraging the LoS path in the A2G channel. By exploiting the specific dual-sequence structure of the sounding signal, this scheme achieves high-fidelity synchronization and accurate CIR retrieval entirely through post-processing, thereby eliminating the reliance on heavy synchronization hardware.

A. Hierarchical Synchronization Strategy

To eliminate timing ambiguities ranging from seconds down to the sub-sample level, we employ a hierarchical synchronization strategy. First, a *coarse alignment* is provided by the 1-PPS GPS trigger, which initiates the measurement burst but leaves a residual timing error of approximately ± 40 ns due to hardware jitter. Second, *symbol-level synchronization* is performed to identify the precise start of each frame. To leverage the ideal periodic autocorrelation properties of the ZC sequence, the cross-correlation $R[l]$ between the received signal $r[k]$ and the local replica $x[n]$ is given by

$$R[l] = \sum_{n=0}^{N_{\text{ZC}}-1} r[l+n] x^*[n]. \tag{10}$$

Robust peak detection is enforced by validating pairs of correlation peaks separated by exactly N_{ZC} samples, corresponding to the dual-ZC structure. This step aligns the data to the symbol level, enabling accurate segmentation for subsequent fine-grained processing.

B. System Response Calibration and CIR Estimation

To isolate the true channel characteristics, the hardware system response $H_{\text{sys}}[v]$—characterized via back-to-back (B2B) calibration—must be deconvolved from the measurements. We perform frequency-domain deconvolution combined with coherent averaging of the dual-ZC segments to suppress noise. The calibrated, time-varying CIR snapshot $h_i[n]$ is subsequently reconstructed through an Inverse Fast Fourier Transform (IFFT), yielding

$$h_i[n] = \mathcal{F}^{-1}\left\{ \frac{R_{i,1}[v] + R_{i,2}[v]}{2H_{\text{sys}}[v]} \right\}, \tag{11}$$

where $R_{i,1}[v]$ and $R_{i,2}[v]$ are the frequency representations of the signal segments in the i-th snapshot.

C. Sampling Frequency Offset (SFO)-Induced Drift Correction (Fine STO)

The final and most critical step for non-stationarity analysis is the correction of the SFO. The SFO between unsynchronized oscillators introduces a periodic power and phase fluctuation in the measured CIR [25], [28]. This measurement artifact would otherwise interfere with the analysis of true channel non-stationarity. We propose a two-stage algorithm to estimate and remove this artifact. (a) estimating the fractional STO (FSTO) for each snapshot, and (b) modeling the SFO-induced linear drift across the burst.

a) High-Precision FSTO Estimation: To achieve sub-sample accuracy, we reconstruct a high-resolution, continuous-time representation of the CIR, $h_{\text{recon},i}(\tau)$, from its discrete samples $h_i[n]$ using Whittaker-Shannon (sinc) interpolation [29]. The reconstructed signal is given by

$$h_{\text{recon},i}(\tau) = \sum_n h_i[n] \text{sinc}\left(\frac{\tau}{T_s} - n\right), \tag{12}$$

where τ is the continuous delay. In practice, this is implemented by upsampling the discrete CIR by an oversampling factor. By locating the peak of $|h_{\text{recon},i}(\tau)|$, the peak time $\hat{\tau}_{\text{peak},i}$ for the i-th CIR with sub-sample precision is obtained. The corresponding FSTO estimate, $\hat{\delta}_i$, is then calculated as

$$\hat{\delta}_i = (\hat{\tau}_{\text{peak},i}/T_s) - \lfloor \hat{\tau}_{\text{peak},i}/T_s \rceil, \tag{13}$$

where $\lfloor \cdot \rceil$ denotes the operation of rounding to the nearest integer.

b) SFO-Induced STO Drift Modeling via Linear Regression: The subsequent processing stage characterizes the constant SFO-induced drift over the 40 ms burst. To mitigate severe estimation errors caused by transient LoS occlusions, a data-space outlier rejection filter is introduced prior to phase unwrapping. Since the true physical clock drift is linear, the first-order differences of adjacent estimates, $\Delta\hat{\delta}_i = \hat{\delta}_{i+1} - \hat{\delta}_i$, exhibit only marginal predictable variations. Anomalous frames where $|\Delta\hat{\delta}_i|$ exceeds a statistical threshold are identified and purged from the dataset.

The cleaned FSTO sequence is subsequently unwrapped into $\{d_i\}$. However, our B2B measurements confirmed that $\{d_i\}$ still contains periodic artifacts inherent to the sinc-based peak-finding method. To filter these artifacts and extract the underlying physical drift, we apply a constrained linear least-squares fit to $\{d_i\}$. First, a baseline slope a_{b2b} is estimated from B2B data, exploiting the period of sliding correlation peaks [25]. A physically plausible search range $[a_{\min}, a_{\max}]$ (e.g., $a_{\text{b2b}}\pm 10\%$) is defined. This physical constraint is used to robustly fit the unwrapped, outlier-free data $\{d_i\}$ to the linear model $\delta(t_i) = a \cdot t_i + b$:

$$(\hat{a}, \hat{b}) = \arg\min_{a,b} \sum_{i=1}^{M} [d_i - (at_i + b)]^2 \quad \text{s.t.} \quad a \in [a_{\min}, a_{\max}]. \tag{14}$$

Algorithm 1 Pure-Algorithmic Synchronization Framework

Require: Received signal $r[n]$, reference ZC sequence $x[n]$, calibrated hardware response $H_{\text{sys}}[v]$
Ensure: Synchronized CIR snapshots
Coarse synchronization using the 1-PPS trigger.
Detect dual-ZC correlation peaks.
Segment the received burst into snapshots.
for each snapshot **do**
    Remove hardware response.
    Estimate CIR by frequency-domain deconvolution.
    Estimate FSTO $\hat{\delta}_i$ using sinc interpolation.
end for
Calculate first-order differences $\Delta\hat{\delta}_i = \hat{\delta}_{i+1} - \hat{\delta}_i$.
Purge anomalous FSTO estimates exceeding a statistical threshold.
Unwrap the cleaned FSTO sequence.
Estimate SFO-induced linear drift using constrained linear regression.
for each valid snapshot **do**
    Apply frequency-domain phase correction.
end for
return Synchronized CIR snapshots.

The modeled drift $\delta_{\text{fit}}(t_i) = \hat{a}t_i + \hat{b}$ is then applied as a phase correction in the frequency domain, yielding a fully synchronized CIR dataset free from hardware-induced non-stationarity.To provide a comprehensive overview of the proposed methodology, the complete pure-algorithmic synchronization framework is summarized in Algorithm 1.

D. Applicability and Limitations

The proposed synchronization framework estimates SFO-induced linear drift by tracking a dominant propagation path that remains stable over a short observation interval (e.g., 40 ms). This requirement aligns well with low-altitude A2G channels, where a persistent LoS component—or a strong, stable NLoS component in LoS-obstructed scenarios—naturally serves as a reliable synchronization reference. Consequently, synchronization performance depends critically on the continuous availability of this dominant path; intermittent blockages or severe fading in the absence of a stable multipath component can degrade peak-tracking accuracy and introduce residual synchronization errors.

Although these extreme propagation conditions define the practical operating boundaries of the proposed method (a detailed boundary analysis is provided in Section VI-F), the elimination of atomic clocks significantly reduces payload weight and hardware complexity. Ultimately, this framework offers a highly practical and effective synchronization solution for lightweight UAV channel sounding systems.

V. DATA ANALYSIS METHODOLOGY

The comprehensive preprocessing pipeline in Section IV yields a set of high-quality, time-varying CIR snapshots, $h_i[n]$, serving as the data foundation for subsequent analysis. This section details the methodology for channel characterization. Guided by the theoretical model established in Section II, we derive analytical expressions for key channel parameters and apply them to extract features from the measurement data. This process transforms raw observations into quantifiable channel statistics, directly supporting the in-depth analysis of non-stationary channel behaviors in Section VI.

A. Large-Scale Path Loss Characterization

The first step in characterizing the channel is to extract the large-scale path loss $\overline{PL}[s]$ from the calibrated CIR samples. To explicitly reveal the impact of the APC effect on the average received power, it is necessary to eliminate the effects of small-scale fading. Specifically, the instantaneous channel power gain $G_p[i]$ for the i-th snapshot is first computed by summing the power gain of all resolved multipath delay taps within each CIR frame, i.e.,

$$G_p[i] = \sum_n |h_i[n]|^2. \tag{15}$$

By substituting (1) into (15), the instantaneous channel power is resolved into the LoS component power, the NLoS component power, and a coherent cross-term representing their interaction

$$\begin{aligned} G_p[i] = \sum_n \Omega(t_i) \Bigg(& \frac{K(t_i)}{K(t_i)+1} |h_{\text{LoS},i}[n]|^2 \\ & + \frac{1}{K(t_i)+1} |h_{\text{NLoS},i}[n]|^2 \\ & + \frac{2\sqrt{K(t_i)}}{K(t_i)+1} \text{Re}\big\{ h_{\text{LoS},i}[n] h^*_{\text{NLoS},i}[n] \big\} \Bigg). \end{aligned} \tag{16}$$

In typical A2G scenarios, wideband signals possess high time-domain resolution, enabling a clear distinction between LoS and NLoS components. Since the LoS path and NLoS multipath components are distributed across non-overlapping intervals along the delay axis, they exhibit mutual orthogonality and statistical independence in the time domain [19]. This orthogonality ensures the absence of coherent interference during power summation, effectively rendering the complex cross-terms zero. Consequently, the instantaneous power gain for the i-th snapshot can be simplified as the linear summation of the LoS power and the total NLoS power. By integrating the physical LoS model from (3) with the NLoS model from (9), the complete expression for the instantaneous channel power gain is derived as

$$\begin{aligned} G_p[i] = & \frac{\Omega(t_i) K(t_i)}{K(t_i)+1} \Big[\mathcal{A}_{\text{GS}}(\theta_a(t_i)) \mathcal{A}_{\text{UAV}}(\theta_a(t_i) + \psi(t_i)) \Big]^2 \\ & + \frac{\Omega(t_i)}{K(t_i)+1} \sum_{n=1}^{N_{\text{cl}}} \eta_n^2 \mathcal{A}_n^2, \end{aligned} \tag{17}$$

where $\Omega(t_i)$, $K(t_i)$, $\theta_a(t_i)$, and $\psi(t_i)$ denote the instantaneous average channel gain, the Rician K-factor, the static off-boresight angle, and the attitude deviation (wobbling angle) at the i-th snapshot, respectively. The large-scale power gain $\overline{G_p}[s]$ is determined by calculating the arithmetic mean of

M instantaneous snapshots $G_p[i]$ captured within the s-th measurement burst

$$\overline{G_p}[s] = \frac{1}{M}\sum_{i=1}^{M} G_p[i]. \tag{18}$$

To investigate the impact of APC on channel characteristics in depth, this section adopts a local stationarity assumption for the propagation delay, geometric off-boresight angle, and Rician K-factor within each measurement burst interval. Consequently, the large-scale power gain can be expressed as

$$\begin{aligned}\overline{G_p}[s] = &\frac{\Omega_s K_s}{K_s+1}\mathcal{A}^2_{\text{GS}}(\theta_{a,s})\left(\frac{1}{M}\sum_{i=1}^{M}\mathcal{A}^2_{\text{UAV}}(\theta_{a,s}+\psi(t_i))\right)\\ &+\frac{\Omega_s}{K_s+1}\sum_{n=1}^{N_{\text{cl}}}\eta_n^2\mathcal{A}_n^2,\end{aligned} \tag{19}$$

where Ω_s, K_s, and $\theta_{a,s}$ denote the local average channel gain, the local Rician K-factor, and the local static off-boresight angle within the s-th measurement burst, respectively. To provide a quantitative analysis of how UAV attitude fluctuations impact large-scale gain, the first-order Taylor expansion of the antenna gain function $\mathcal{A}_{\text{UAV}}(\theta_{a,s}+\psi(t_i))$ is incorporated into the gain expression, leading to the expanded form

$$\begin{aligned}\mathcal{A}^2_{\text{UAV}}(\theta_{a,s}+\psi(t_i)) \approx\ &\mathcal{A}^2_{\text{UAV}}(\theta_{a,s})\\ &+2\,\mathcal{A}_{\text{UAV}}(\theta_{a,s})\,\mathcal{A}'_{\text{UAV}}(\theta_{a,s})\,\psi(t_i)\\ &+\left[\mathcal{A}'_{\text{UAV}}(\theta_{a,s})\right]^2\psi(t_i)^2.\end{aligned} \tag{20}$$

Following the wobbling model in (6), $\psi(t)$ is characterized as a zero-mean sinusoidal process. Given a sufficiently large sample size M, the time-averaged value of the linear perturbation term vanishes, i.e., $\frac{1}{M}\sum_{i=1}^{M}\psi(t_i)\approx 0$, while the time-averaged power of the wobbling component satisfies $\frac{1}{M}\sum_{i=1}^{M}\psi(t_i)^2\approx\frac{1}{2}\psi^2_{\max}$. Leveraging these statistical properties, the linear cross-term is eliminated during the averaging process, and the average squared antenna gain simplifies to

$$\begin{aligned}&\frac{1}{M}\sum_{i=1}^{M}\mathcal{A}^2_{\text{UAV}}(\theta_{a,s}+\psi(t_i))\\ \approx&\mathcal{A}^2_{\text{UAV}}(\theta_{a,s})+\frac{1}{2}\left(\mathcal{A}'_{\text{UAV}}(\theta_{a,s})\right)^2\psi^2_{\max}.\end{aligned} \tag{21}$$

Thus, the analytical expression for the large-scale power gain becomes

$$\begin{aligned}\overline{G_p}[s] \approx &\frac{\Omega_s K_s}{K_s+1}\mathcal{A}^2_{\text{GS}}(\theta_{a,s})\\ &\cdot\left[\mathcal{A}^2_{\text{UAV}}(\theta_{a,s})+\frac{1}{2}\left(\mathcal{A}'_{\text{UAV}}(\theta_{a,s})\right)^2\psi^2_{\max}\right]\\ &+\frac{\Omega_s}{K_s+1}\sum_{n=1}^{N_{\text{cl}}}\eta_n^2\mathcal{A}_n^2.\end{aligned} \tag{22}$$

Finally, the large-scale path loss $\overline{PL}[s]$ (in dB) for that measurement burst is calculated by converting the averaged large-scale gain from linear scale to dB. The resulting definition and approximation are given by (23) on the next page.

B. Temporal Autocorrelation Function (ACF)

Although large-scale path loss reflects the average power distribution within a measurement burst interval, as a long-term statistical measure, it cannot capture the rapid channel dynamics induced by the APC effect. To thoroughly evaluate such microscopic time-varying behaviors, it is essential to further investigate the temporal correlation of the channel. This section derives the temporal ACF with the aim of quantifying the dependency between channel responses at different observation instants and revealing their fluctuation characteristics in the time domain.

Based on the local stationarity assumption, the correlation between CIRs at different time instants is given by

$$R_h(t;\Delta t) = \mathbb{E}[h(t)h^*(t+\Delta t)], \tag{24}$$

where $\mathbb{E}[\cdot]$ denotes the statistical expectation operator, and $(\cdot)^*$ represents the complex conjugate operation.

In A2G communication scenarios, the LoS and NLoS components are statistically independent, which leads to the vanishing of the cross-terms in the expansion of the expectation. Concurrently, based on the local stationarity assumption established through the analysis of the APC effect—where the propagation delay, geometric angles, and Rician K-factor are approximately constant within each measurement burst—the large-scale parameters $\Omega(t)$ and $K(t)$ are also assumed to be invariant over the observation interval Δt. Accordingly, the time autocorrelation function can be simplified as a weighted sum of the individual autocorrelation functions of the two components, expressed as

$$R_h(t;\Delta t) = \frac{\Omega K}{K+1}R_{\text{LoS}}(t;\Delta t)+\frac{\Omega}{K+1}R_{\text{NLoS}}(t;\Delta t), \tag{25}$$

where $R_{\text{LoS}}(t;\Delta t)$ and $R_{\text{NLoS}}(t;\Delta t)$ represent the temporal autocorrelation functions of the LoS and NLoS components, respectively. Here, Ω and K signify the local average channel gain and the Rician K-factor within the current measurement burst. By incorporating the influence of the antenna radiation pattern and assuming a constant Doppler shift $f_{\text{d},0}$, substituting (3) into the expression for the LoS component $R_{\text{LoS}}(\Delta t)$, it can be further expanded as

$$\begin{aligned}R_{\text{LoS}}(t;\Delta t) = \mathbb{E}\Big[&\mathcal{A}_{\text{UAV}}(\theta_a+\psi(t))\mathcal{A}_{\text{UAV}}(\theta_a+\psi(t+\Delta t))\Big]\\ &\cdot\mathcal{A}^2_{\text{GS}}(\theta_a)\,e^{-j2\pi f_{\text{d},0}\Delta t},\end{aligned} \tag{26}$$

where θ_a denotes the local static off-boresight angle. To solve the expectation term in (26), we use the first-order Taylor expansion of the antenna pattern from (7). Substituting this expansion yields the approximation given in (27). Since the jitter is modeled as a sinusoidal periodic function (6) with a random phase ϕ_0 uniformly distributed over $[0,2\pi)$, the jitter autocorrelation function $\mathbb{E}[\psi(t)\psi(t+\Delta t)]$ is given by

$$\mathbb{E}[\psi(t)\psi(t+\Delta t)] \approx \frac{\psi^2_{\max}}{2}\cos(2\pi f_w\Delta t). \tag{28}$$

$$\overline{PL}[s] = -10\log_{10}\left(\overline{G_p}[s]\right)$$
$$\approx -10\log_{10}\left(\frac{\Omega_s}{K_s+1}\right) - 10\log_{10}\left[K_s\,\mathcal{A}^2_{\text{GS}}(\theta_{a,s})\left(\mathcal{A}^2_{\text{UAV}}(\theta_{a,s}) + \frac{1}{2}\left(\mathcal{A}'_{\text{UAV}}(\theta_{a,s})\right)^2\psi^2_{\max}\right) + \sum_{n=1}^{N_{\text{cl}}}\eta_n^2\mathcal{A}_n^2\right]. \tag{23}$$

$$\mathbb{E}\left[\mathcal{A}_{\text{UAV}}(\theta_a+\psi(t))\mathcal{A}_{\text{UAV}}(\theta_a+\psi(t+\Delta t))\right] \approx \mathbb{E}\left[\left(\mathcal{A}_{\text{UAV}}(\theta_a)+\mathcal{A}'_{\text{UAV}}(\theta_a)\psi(t)\right)\cdot\left(\mathcal{A}_{\text{UAV}}(\theta_a)+\mathcal{A}'_{\text{UAV}}(\theta_a)\psi(t+\Delta t)\right)\right]$$
$$\approx \mathcal{A}^2_{\text{UAV}}(\theta_a) + \mathcal{A}_{\text{UAV}}(\theta_a)\mathcal{A}'_{\text{UAV}}(\theta_a)\mathbb{E}[\psi(t)] + \mathcal{A}_{\text{UAV}}(\theta_a)\mathcal{A}'_{\text{UAV}}(\theta_a)\mathbb{E}[\psi(t+\Delta t)] + (\mathcal{A}'_{\text{UAV}}(\theta_a))^2\mathbb{E}[\psi(t)\psi(t+\Delta t)]. \tag{27}$$

$$\rho(\Delta t) \approx \frac{K\mathcal{A}^2_{\text{GS}}(\theta_a)e^{-j2\pi f_{\text{d},0}\Delta t}\left[\mathcal{A}_{\text{UAV}}(\theta_a)^2 + \frac{(A'_{\text{UAV}}(\theta_a)\psi_{\max})^2}{2}\cos(2\pi f_w\Delta t)\right] + \sum_{n=1}^{N_{\text{cl}}}\eta_n^2\mathcal{A}_n^2 e^{-j2\pi f_{\text{d},n}\Delta t}}{K\mathcal{A}^2_{\text{GS}}(\theta_a)\left[\mathcal{A}_{\text{UAV}}(\theta_a)^2 + \frac{(A'_{\text{UAV}}(\theta_a)\psi_{\max})^2}{2}\right] + \sum_{n=1}^{N_{\text{cl}}}\eta_n^2\mathcal{A}_n^2}. \tag{32}$$

Therefore, the final autocorrelation expression for the LoS component is obtained as

$$R_{\text{LoS}}(t;\Delta t) \approx \left[\mathcal{A}_{\text{UAV}}(\theta_a)^2 + \frac{(\mathcal{A}'_{\text{UAV}}(\theta_a)\psi_{\max})^2}{2}\cos(2\pi f_w\Delta t)\right] \cdot \mathcal{A}^2_{\text{GS}}(\theta_a)e^{-j2\pi f_{\text{d},0}\Delta t}. \tag{29}$$

Substituting (9) into the autocorrelation function of the NLoS component, and based on the assumptions of local stationarity and uncorrelated scattering, the random phase offsets ϕ_n of each multipath component (induced by reflection interactions) are mutually independent and uniformly distributed over $[0, 2\pi)$. Utilizing this orthogonality, the cross-correlation terms in the expansion cancel out, leaving only the autocorrelation terms where $n = m$, thus leading to the simplified expression which is given by

$$R_{\text{NLoS}}(t;\Delta t) = \sum_{n=1}^{N_{\text{cl}}}\eta_n^2\mathcal{A}_n^2 e^{-j2\pi f_{\text{d},n}\Delta t}. \tag{30}$$

Combining the above results, it can be seen that the autocorrelation functions of both the LoS and NLoS components are independent of time t. Therefore, the analytical expression for the total time-domain autocorrelation function of the A2G channel can be written as

$$R_h(\Delta t) \approx \frac{\Omega K}{K+1}\,\mathcal{A}^2_{\text{GS}}(\theta_a)e^{-j2\pi f_{\text{d},0}\Delta t} \cdot \left[A_{\text{UAV}}(\theta_a)^2 + \frac{(A'_{\text{UAV}}(\theta_a)\psi_{\max})^2}{2}\cos(2\pi f_w\Delta t)\right] + \frac{\Omega}{K+1}\sum_{n=1}^{N_{\text{cl}}}\eta_n^2\mathcal{A}_n^2 e^{-j2\pi f_{\text{d},n}\Delta t}. \tag{31}$$

To further analyze the temporal correlation characteristics of the channel, we calculate the normalized ACF. First, by setting $\Delta t = 0$, the average channel power $R_h(0)$ is obtained. Subsequently, the normalized ACF is defined as $\rho(\Delta t) = R_h(\Delta t)/R_h(0)$. Substituting (31) into this definition and simplifying yields the expression presented in (32).

C. Stationary Interval

Although autocorrelation analysis reveals channel time-varying characteristics at a microscopic level, the high mobility of UAVs induces strong non-stationarity in the A2G channels on a macroscopic scale. This implies that the WSS assumption holds only within limited time windows and is not applicable to the entire flight duration. Therefore, it is necessary to explicitly define the Stationarity Interval (SI) to evaluate the validity range of the aforementioned statistical models. Since the determination of the stationarity interval involves complex numerical computations and it is intractable to derive a closed-form solution, no mathematical derivation is presented in this section.

The key metric for quantifying the degree of channel non-stationarity is the stationarity time, T_{sta}, which delineates the quasi-stationary region where channel statistical properties can be considered approximately invariant [12], [29], [30]. To estimate this parameter, we adopt a classical method based on the correlation of the Average Power Delay Profile (APDP) [30], [31]. This approach mitigates the impact of small-scale fading through averaging operations while effectively capturing intrinsic changes in the channel structure. Specifically, the APDP corresponding to the j-th time snapshot, denoted as $\bar{P}_h(j,n)$, is obtained by averaging the instantaneous power of the calibrated CIR, $h_i[n]$, over a sliding window containing N_w snapshots. Its expression is given by

$$\bar{P}_h(j,n) = \frac{1}{N_w}\sum_{i=j}^{j+N_w-1}|h_i[n]|^2. \tag{33}$$

Next, the similarity between the channel's delay structures at different time instants j_1 and j_2 is quantified using the normalized correlation coefficient $\rho(j_1, j_2)$ [30]. This yields a correlation matrix $R[j_1, j_2] = \rho(j_1, j_2)$, where the coefficient is given by

$$\rho(j_1,j_2) = \frac{\sum_n \bar{P}_h(j_1,n)\bar{P}_h(j_2,n)}{\max\left\{\sum_n \bar{P}_h(j_1,n)^2, \sum_n \bar{P}_h(j_2,n)^2\right\}}. \tag{34}$$

To find an average stationarity duration, the correlation matrix R is averaged along its diagonals to produce an average correlation curve $\mu[m]$ as a function of time lag m,

$$\mu[m] = \text{mean}\{R[j, j+m] | 1 \leq j \leq M' - m\}, \tag{35}$$

where $M' = M - N_w + 1$ is the total number of APDP snapshots. Finally, the stationarity time, $T_{\text{sta}}(\gamma)$, is determined as the maximum duration for which this average correlation remains above a selected threshold γ [30], which is given by

$$T_{\text{sta}}(\gamma) = m_{\max} \Delta t, \tag{36}$$

where $m_{\max}$ is the largest lag index such that $\mu[m'] \geq \gamma$ for all $0 \leq m' \leq m_{\max}$, and Δt is the time interval between CIR snapshots (around 50 μs).

VI. Results and Analysis

Based on the measurement campaign and the theoretical framework established in Section II, this section presents a comprehensive analysis of the A2G channel characteristics. To systematically validate the proposed APC model, we employ a comparative analysis approach, benchmarking measurement data against numerical simulations and analytical results. The analysis focuses on verifying the non-stationary characteristics induced by antenna effects in key channel metrics, including large-scale path loss and temporal stationarity, thereby elucidating the physical mechanism behind the observed stationarity violation.

A. Measurement Scenarios and Simulation Configuration

1) Physical Measurement Setup: The measurement campaign was conducted within a suburban campus environment at Shenzhen University, as depicted in Fig. 5. The propagation scenario comprised a relatively open lawn area, flanked by several multi-story teaching buildings with an approximate height of 40 m. The ground-based RX was stationary at a fixed location, denoted as "RX Position" in the figure. The UAV-mounted TX executed flights along a predefined horizontal trajectory of approximately 50 m, indicated as "TX Trace" in Fig. 5. A constant, low flight speed of approximately 1 m/s was maintained. This low velocity was an intentional methodological choice to minimize the Doppler spread induced by linear motion, thereby isolating the non-stationary effects originating specifically from the antenna's radiation pattern and the UAV's attitude variations. To investigate altitude-dependent channel characteristics, this trajectory was systematically repeated at three distinct altitudes: 20 m, 40 m, and 60 m. This experimental design ensured a dominant LoS path was maintained throughout all measurements, with primary multipath components (MPCs) originating from ground reflections and scattering from the adjacent building facades.

2) Simulation Configuration: To validate the APC model proposed in Section II, both numerical simulations and analytical derivations were configured to replicate the physical measurement parameters. The selection of key parameters was designed to align with hardware specifications and experimental observations:

- **RF and System:** The carrier frequency was set to $f_c = 3$ GHz with a transmission power of 23 dBm. The time-domain sampling rate was set to 100 MHz, providing a delay resolution of 10 ns, consistent with the wideband sounder.
- **Geometry and Motion:** The simulated UAV followed the same horizontal trajectory range ($[3, 28]$ m) at altitudes of $\{20, 40, 60\}$ m with a constant velocity of 1 m/s.
- **Antenna and Channel:** The antenna radiation pattern was modeled using the Bessel J_1 model in (2) with a peak gain angle of $\theta_{\text{peak}} = 38°$. The channel was modeled with a Rician factor of $K = 10$ dB, where the NLoS component was composed of 6 multipath components whose powers decayed from -12 to -22 dB [32], [33].
- **Attitude Dynamics:** To capture the micro-scale instability, the attitude wobbling was modeled with a frequency of $f_w = 10$ Hz and a maximum wobbling amplitude of $\psi_{\max} = 2°$, following the empirical simulation configuration reported in [16] for rotary-wing UAVs. This choice ensures consistency with representative UAV channel modeling studies.

The above parameter settings ensure that the analytical predictions, simulation results, and empirical data presented in the subsequent subsections are directly comparable on a unified basis.

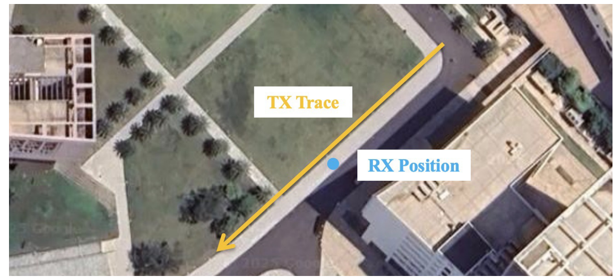

Fig. 5. Satellite view of the A2G measurement scenario at Shenzhen University.

B. PDP and Path Loss

Fig. 6 illustrates the time-varying PDPs measured along the horizontal trajectory at three distinct flight altitudes. Based on the propagation model $d = c\tau$, the dominant LoS path exhibits significant geometric delay variations. As the slant range evolves, the LoS delay shifts from approximately 80 ns at an altitude of 20 m to roughly 200 ns at 60 m. Furthermore, the multipath structure displays a distinct altitude-dependent trend: both the maximum excess delay and the overall delay spread increase with altitude. This is attributed to the expansion of "propagation visibility", where higher altitudes enable signals to interact with more distant scatterers that are typically obstructed by adjacent buildings at lower altitudes.

A critical phenomenon is observed across all altitudes: when the UAV is positioned directly above the receiver area, the LoS path power attenuates significantly, manifesting as a distinct low-power "dark band" at the center of the PDPs. This anomaly is directly attributable to the non-omnidirectional antenna radiation pattern (Fig. 1). When the UAV is at the zenith position, the LoS path aligns with the antenna's direction of minimum gain (i.e., the nadir gain null), resulting in a drastic reduction in received energy.

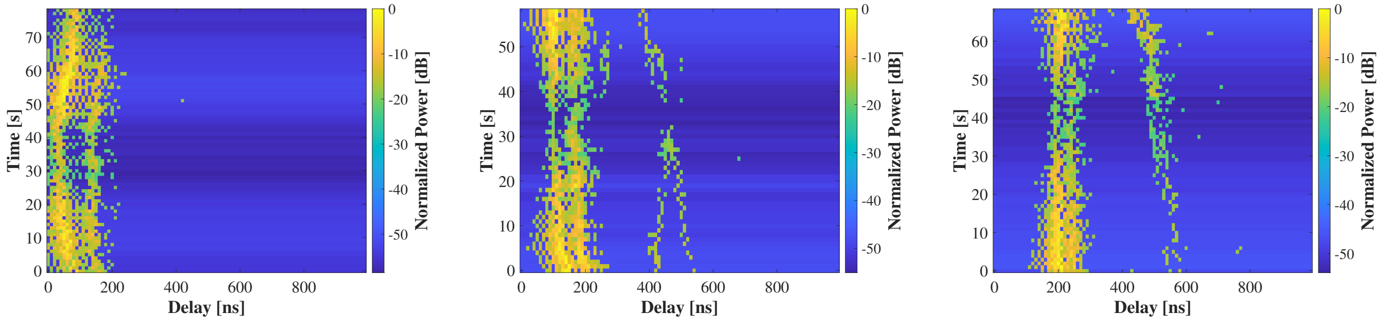

(a) Altitude: 20 m (b) Altitude: 40 m (c) Altitude: 60 m

Fig. 6. Time-varying PDPs measured along the horizontal trajectory at different altitudes (20 m, 40 m, and 60 m).

To quantitatively analyze this antenna effect and validate the APC model proposed in Section II, Fig. 7 presents the large-scale path gain along the flight trajectory, comparing results from empirical measurements, numerical simulations, and analytical derivations. The results demonstrate a high degree of consistency among all data, providing robust verification of the established model's accuracy.

Specifically, the comparison at the 20 m altitude (Fig. 7a) clearly reveals a characteristic non-monotonic trend of an initial increase followed by a decrease. Although path gain typically increases as the distance decreases (as the UAV approaches from 28 m to 13 m), both the analytical derivation and measurement data indicate that as the UAV closes in further (from 13 m to 3 m), the path gain conversely drops sharply by approximately 8–10 dB. This reversal phenomenon is precisely captured by the analytical model, confirming that when the propagation path enters the antenna gain null region, the rapid attenuation induced by the radiation pattern overwhelms the free-space path gain resulting from the reduced geometric distance.

At higher altitudes (40 m and 60 m), the geometric width of the antenna-induced attenuation cone projected on the ground increases significantly. Both analytical derivation and simulation results accurately predict this expansion trend: the entire 60 m flight trajectory lies almost completely within the low-gain region, preventing the gain from recovering to the high levels observed at the periphery of the 20 m altitude. The large-scale envelope of the measurement data closely follows the analytical derivation curve, and this strong consistency fully validates that the proposed APC model correctly decouples and reproduces the physical interaction between the UAV flight trajectory and the time-varying antenna gain.

It is worth noting that the analytical derivation clearly elucidates the power variation trend determined by geometry and antenna characteristics, while the numerical simulation further verifies the stochastic features under this trend. Within the antenna-induced attenuation region, the suppression of the dominant LoS path implicitly elevates the relative power weight of NLoS components. Given that the primary driver of this phenomenon has been confirmed as the temporal instability caused by APC, the remainder of this paper will focus on the analysis of time-domain non-stationarity based on this physical mechanism.

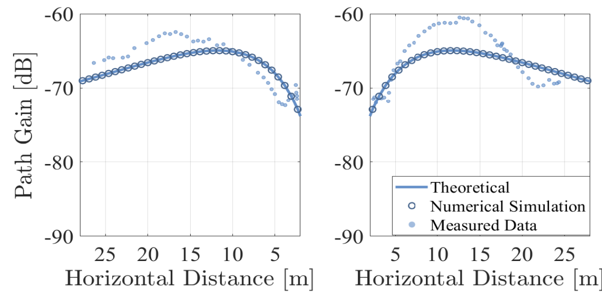

(a) Altitude: 20 m

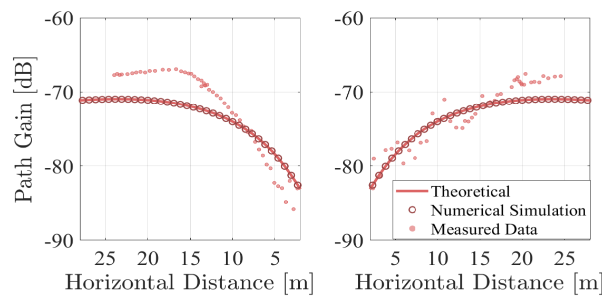

(b) Altitude: 40 m

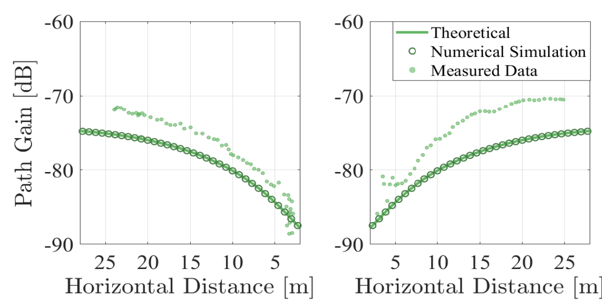

(c) Altitude: 60 m

Fig. 7. Large-scale received power distribution along the horizontal trajectory based on analytical derivations, numerical simulations, and experimental measurements.

C. Temporal Autocorrelation Analysis and Model Verification

This section investigates the temporal autocorrelation characteristics of the A2G wireless channel under the influence of the APC. To ensure methodological rigor, the proposed analytical model is validated against both Monte Carlo numerical simulations and field-based empirical measurements. Furthermore, the impact of the power weighting mechanism on channel coherence within the beam null region is analyzed. Fig. 8 presents a detailed comparison of the normalized temporal ACF magnitude, $|\rho(\Delta t)|$, derived from the analytical model, simulations, and measurements. The evaluation focuses on two representative spatial regimes: the Main Lobe ($\theta = 38°$), corresponding to maximal beam gain, and the Beam Null Edge ($\theta \approx 5°$), characterized by a steep gain gradient. Overall, the analytical predictions exhibit a high degree of consistency with both the simulation and measurement data, confirming the model's accuracy across distinct spatial domains. A deeper analysis reveals that in the Main Lobe region, the ACF maintains a value near unity, indicating strong temporal stability. This stability is attributed to the flat antenna gain profile at the peak plateau, where the gradient $A'(\theta)$ approaches zero. Consequently, angular deviations induced by mechanical jitter translate into negligible amplitude fluctuations, thereby preserving the strong coherence of the dominant LoS component.

However, a counter-intuitive phenomenon is observed in the beam null edge region. Although the antenna gain slope in this narrow zone ($\pm 5°$) is relatively steep, which theoretically induces significant relative amplitude fluctuations in the LoS component-the measured total channel correlation does not collapse as expected but instead maintains a relatively high level. This phenomenon is well explained by the proposed Power Weighting Mechanism. While the steep gradient in the deep null indeed causes drastic relative jumps in the LoS component, the simultaneous deep attenuation of the antenna pattern significantly reduces the power weight of the LoS component, dropping its absolute power to a level comparable to or even lower than that of the NLoS component. As indicated by (25), the total ACF is essentially a weighted superposition of the LoS and NLoS ACFs. When the LoS component no longer occupies a dominant power position, the weight of its highly volatile ACF term in the total summation is drastically suppressed. Consequently, the time-varying characteristics of the total channel manifest the behavior of the more stable NLoS component. Since the decorrelation rate of the NLoS component is governed by the relatively slow Doppler frequency shift rather than the fast mechanical jitter, the total ACF retains high coherence even in the geometrically unstable null region. The excellent agreement between measurement data and theoretical curves confirms that the proposed model correctly decouples the complex interaction between the drastic fluctuations of the LoS component and the power contribution ratios of the multipath components.

D. Temporal Stationarity and Antenna-Induced Instability

The path loss analysis indicated anomalous power variations caused by the antenna radiation pattern. We now investigate how this phenomenon affects the temporal stationarity of the channel.

1) Macro-Scale Stationarity Collapse and Model Validation: To quantify the stability of the channel structure, we employ the APDP correlation method (with parameter $\gamma =$

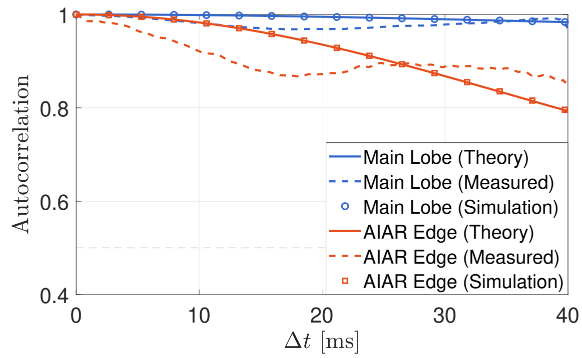

Fig. 8. Comparison of temporal ACF across different beam regions (main lobe and beam null edge): Validation through theoretical derivation, Monte Carlo simulations, and experimental data.

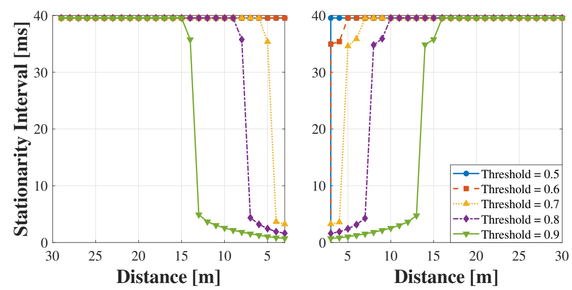

(a) Simulation results

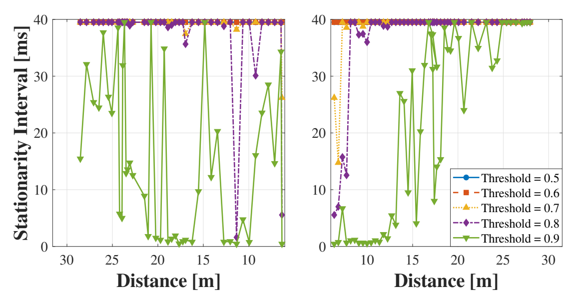

(b) Measurement results

Fig. 9. Comparative analysis of channel stationarity interval thresholds along a horizontal trajectory at 40 m altitude.

0.8) to estimate the stationarity time T_{sta}. The analysis results indicate that the theoretical upper limit of the channel baseline stability is $T_{\text{sta, max}} \approx 40$ ms, which represents the maximum duration the system can theoretically maintain a stationary state. Since the APDP is estimated using a sliding window of length $N_w = 10$ snapshots (with a step size of 1 snapshot), the maximum stationarity interval that can be captured by this method is 39.5 ms. However, the experimental results in Fig. 10 reveal a critical phenomenon: a significant "consistency collapse of stationarity" occurs across all tested altitudes. In the low-elevation regions, the channel exhibits high stability ($T_{\text{sta}} \approx 40$ ms). However, as the UAV enters the near-nadir AIAR, T_{sta} drops precipitously to below 15 ms. Crucially, this non-stationary region aligns closely with the antenna's gain null, implying the instability is transceiver-induced rather than environment-driven.

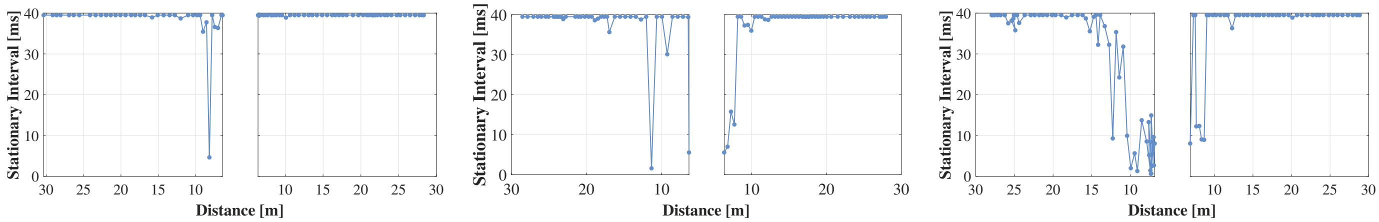

(a) Altitudes: 20 m (b) Altitudes: 40 m (c) Altitudes: 60 m

Fig. 10. Channel stationary interval (based on an APDP correlation threshold of $\gamma = 0.8$) along the horizontal trajectory.

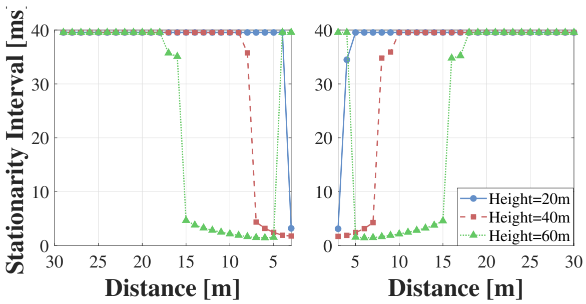

Fig. 11. Comparison of simulated stationarity time (T_{sta}) versus horizontal distance across different flight altitudes, validating the proposed APC model.

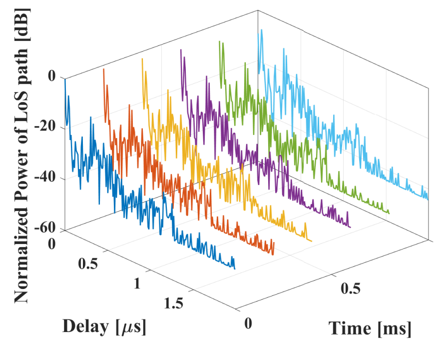

Fig. 12. Micro-scale evolution of the PDP in the non-stationary region (Altitude: 40 m, Horizontal Distance: 7.25 m) over a 1 ms interval, highlighting rapid LoS path power fluctuations with minimal spatial change.

To validate the physical mechanism, Fig. 11 presents the simulated stationarity time derived from the proposed APC model. The simulation results exhibit a high degree of agreement with the measurements in Fig. 10, accurately reproducing both the sharp drop in the null region and the stability in the far field. This consistency confirms that the observed non-stationarity is effectively captured by the coupling between the antenna's gain gradient and the UAV's attitude dynamics.

To rigorously justify the selection of the APDP correlation threshold γ and demonstrate that the observed stationarity collapse is not a parameter-tuning artifact, a sensitivity analysis is conducted across a spectrum of γ values. The results, illustrated in Figs. 9(a) and (b) for both simulation and measurement, indicate that the stationarity assessment is highly threshold-dependent. Specifically, permissive thresholds (e.g., $\gamma \in \{0.5, 0.6\}$ and partially 0.7) fail to capture the collapse, thereby masking the non-stationary behavior of the channel. Conversely, an overly conservative threshold ($\gamma = 0.9$) yields a premature indication of non-stationarity, triggering the collapse before the UAV reaches the primary antenna gain null.

In contrast, a threshold of $\gamma = 0.8$ identifies the onset of stationarity collapse at a horizontal distance of approximately 7 m, which geometrically corresponds to an elevation angle of roughly $10°$. This angle aligns precisely with the steep roll-off region of the antenna radiation pattern. Consequently, $\gamma = 0.8$ serves as the optimal choice and establishes a physically meaningful mapping from the channel stationarity metrics to the actual physical boundaries of transceiver performance degradation.

2) Micro-Scale Instability Mechanism: Fig. 12 details the PDP evolution over a mere 1.0 ms interval. Despite negligible spatial displacement, the LoS power fluctuates by nearly 9 dB (Table III). It is important to note that while the onboard IMU (60 Hz) effectively captures the macroscopic attitude instability, it is bandwidth limited and cannot directly resolve high-frequency micro-vibrations inherent to rotary-wing propulsion. However, the observed channel dynamics provide indirect but compelling evidence of their existence. Within the AIAR, the antenna's gain gradient is extremely steep; physically, this acts as a sensitivity amplifier, where even minute, sub-degree angular jitters—imperceptible to standard IMU sampling—are translated into rapid fluctuations in the received signal power.

TABLE III
INSTANTANEOUS POWER FLUCTUATIONS OF THE LOS PATH

Time t [ms]	0.0	0.2	0.4	0.6	0.8	1.0
Normalized Power of LoS Path [dB]	0.00	-0.80	-1.75	-3.91	-6.19	-8.99

3) Quantification via Normalized Dominant Path Power: To systematically quantify this instability, we propose the distribution of the normalized dominant path power (NDPP). For the s-th measurement burst, all samples are strictly time-aligned using the LoS path as the reference. Consequently, the delay index of the dominant path, n_{dom}, is defined as the fixed delay bin of this aligned LoS path across all M snapshots. This fixed-index approach ensures that the NDPP metric captures pure amplitude fluctuations induced by the APC effect, effectively eliminating path-switching artifacts. Finally, the instantaneous power is normalized by the peak

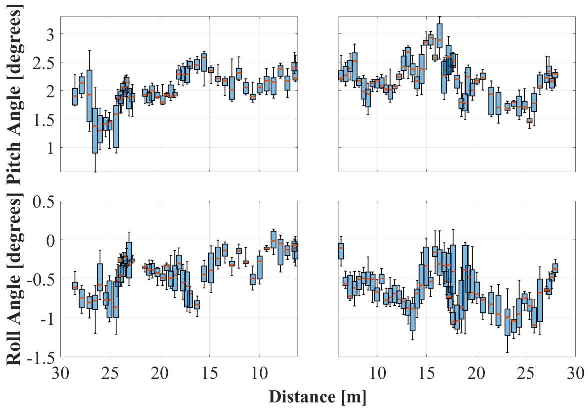

Fig. 13. Recorded UAV attitude dynamics (pitch and roll) during the horizontal flight trajectory.

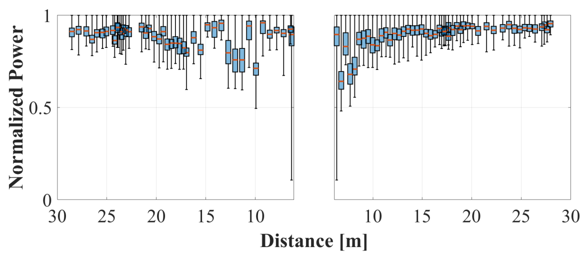

Fig. 14. Statistical distribution of the NDPP within each 40 ms measurement burst along the trajectory.

power within that burst:

$$P_{\text{norm}}^{(s)}[i] = \frac{|h_i[n_{\text{dom}}]|^2}{\max_{k\in[1,M]}|h_k[n_{\text{dom}}]|^2}, \quad i = 1, \ldots, M. \tag{37}$$

The statistical distribution of $P_{\text{norm}}^{(s)}$ is visualized in Fig. 14. The results show a strong negative correlation with T_{sta}: in stable low-elevation regions, values cluster near 1.0 due to the flat antenna gain; conversely, in the near-nadir region, the boxplots expand to cover the full dynamic range. This statistically confirms that the antenna's anisotropy amplifies micro-scale wobbling into macro-scale non-stationarity.

E. Expansion of Non-Stationary Region under High-Dynamic attitude

Real-world UAV communications often face environmental stressors like strong winds, inducing significant mechanical wobbling. We hypothesize that this instability interacts with the antenna pattern to expand the non-stationary region. To verify this, we conducted comparative measurements under simulated "high-wobbling" conditions in two distinct spatial scenarios.

1) Scenario A: Near-Nadir Region (Expansion Effect): First, the UAV retraced the 40 m trajectory with induced swinging. Fig. 15a shows a substantial increase in attitude instability compared to stable flight (variations within $\pm 0.5°$), with pitch and roll variations spanning approximately $25°$ and $10°$, respectively.

Comparing the resulting stationarity time T_{sta} (Fig. 15b) with stable flight (Fig. 10b) reveals a significant expansion

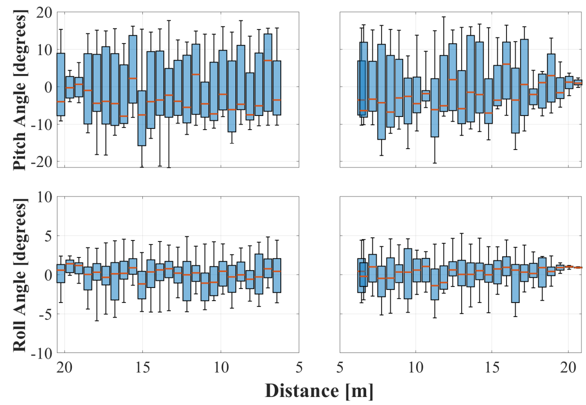

(a) Boxplots of pitch and roll angles showing significantly increased variance compared to stable flight.

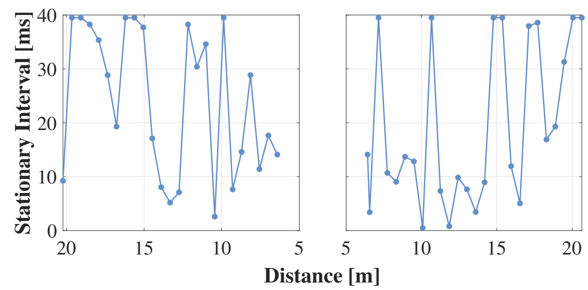

(b) The non-stationary region (where $T_{\text{sta}} < 15$ ms) expands to approximately 20 m, significantly wider than in the stable flight scenario.

Fig. 15. Impact of high-dynamic attitude variations in the near-nadir region (Altitude: 40 m).

of the non-stationary zone. While originally confined to a narrow nadir cone (< 10 m), the region of rapid fluctuations ($T_{\text{sta}} < 15$ ms) now extends to 20 m. This confirms that larger attitude variations effectively broaden the antenna's null, causing the LoS path to sweep into the high-gradient attenuation region at larger horizontal distances.

2) Scenario B: Mechanism Verification in Low-Elevation Region: To definitively distinguish the proposed APC effect from traditional geometric-based assumptions, we conducted a control experiment in the low-elevation region (horizontal distance: 55–75 m). In this region, the LoS path aligns with the flat main lobe of the antenna, where the gain gradient is negligible ($\mathcal{A}' \approx 0$).

If the non-stationarity were primarily driven by the micro-scale spatial displacement of the antenna (as suggested in existing geometric models), the severe wobbling observed in Fig. 16a (pitch variation $\approx 20°$) should still induce channel instability. However, as shown in Fig. 16b, the channel remains highly stationary (T_{sta} maintained at approximately 40 ms).

This contrast provides conclusive evidence for the APC mechanism: high-dynamic wobbling triggers stationarity collapse *only* when it couples with a steep gain gradient (as in the near-nadir region). The physical displacement caused by wobbling is, by itself, insufficient to destroy channel stationarity in typical A2G scenarios.

3) Scenario C: High-Mobility Cruise and Baseline Model Comparison: Previously, a low UAV velocity (1 m/s) iso-

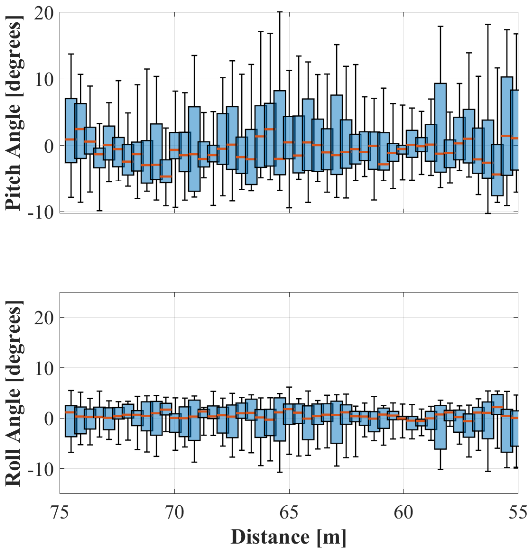

(a) Pitch and yaw angles showing high-intensity wobbling.

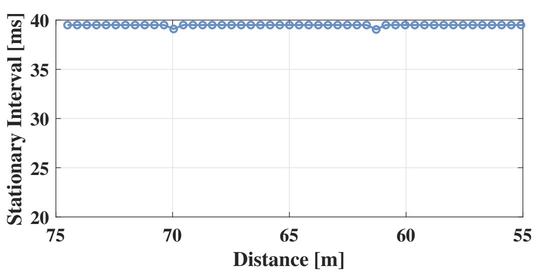

(b) Corresponding stationarity time (T_{sta}) maintaining stability at the measurement ceiling.

Fig. 16. Decoupling experiment in the low-elevation region (Distance: 55–75 m).

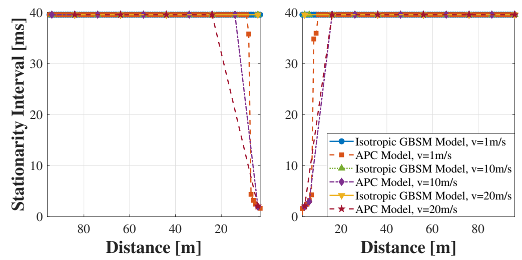

Fig. 17. Simulated local stationarity intervals of isotropic GBSM and APC model at 1, 10, and 20 m/s.

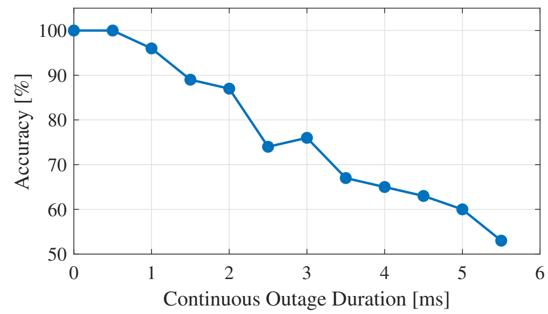

Fig. 18. Estimation accuracy rate of the synchronization algorithm under varying continuous LoS outage durations.

lated the antenna pattern coupling (APC) effect from motion-induced Doppler spread. To assess whether high mobility obscures this effect and highlight current modeling limitations, Fig. 17 compares local stationarity intervals at 1, 10, and 20 m/s between the traditional isotropic GBSM baseline [34] and the proposed APC model.

Results confirm the APC effect dominates across all velocities. The isotropic baseline maintains a stable, near-maximum stationarity interval, proving that spatial displacement and Doppler spread alone cannot trigger the observed stationarity collapse. Conversely, the proposed APC curves—even at 20 m/s—degrade sharply in the near-nadir region. This validates that during near-nadir operations, the dynamic coupling of micro-scale wobbling and antenna anisotropy remains the predominant source of channel non-stationarity, fundamentally overshadowing the impact of horizontal cruise speed.

F. Robustness and Failure Boundary under Transient LoS Blockage

To evaluate the framework's robustness against transient LoS blockages, consecutive blockages are artificially introduced. While an abnormal STO rejection procedure ensures reliable drift fitting in (14) by removing unreliable estimates, prolonged blockages leave insufficient valid STOs. This results in incomplete STO compensation and CIR misalignment, which introduces incoherent components into the APDP and consequently underestimates T_{sta}.

To quantify this limit, transient blockages were simulated on a stable dataset (reference T_{sta} = 40 ms). As shown in Fig. 18, estimation accuracy is 100% for blockages $<$ 0.5 ms and remains robust at 87% for 1–2 ms. Beyond 2 ms, accuracy degrades rapidly (e.g., 74% at 2.5 ms, 53% at 5.5 ms), indicating that 2 ms of consecutive LoS blockage constitutes the practical failure boundary of the proposed framework.

VII. Conclusion

This work identifies and explains a fundamental yet previously neglected cause of non-stationarity in low-altitude A2G channels—the APC effect. Through a custom lightweight channel sounder and an algorithmic synchronization scheme, we captured a sharp stationarity collapse when the LoS path entered the antenna's nadir attenuation region. Our analysis shows that the steep gain gradient around the antenna null acts as a sensitivity amplifier, converting micro-scale UAV wobbling into pronounced LoS power fluctuations. We developed an APC-based analytical model and derived its key statistical properties, including the temporal ACF. Numerical simulations show agreement with the theoretical predictions and measurement data, validating the accuracy of the proposed framework. We also introduced the NDPP metric to quantify this instability. Field experiments across multiple altitudes and wobbling conditions validate that: (i) near-nadir non-stationarity is dominated by antenna pattern gradients rather than geometric displacement, and (ii) low-elevation regions remain highly stationary even under severe attitude variations. These results overturn the conventional distance-driven stationarity assumption and highlight the critical role of antenna design and installation in ensuring reliable UAV communication—particularly for near-nadir operations central to emerging low-altitude applications.

Finally, while the proposed APC mechanism provides useful insights for antenna selection and deployment in low-altitude A2G communications, several limitations of this work deserve further investigation. Antennas with smoother radiation patterns may alleviate the attitude-induced non-stationarity, albeit at the expense of antenna gain and coverage. Moreover, the applicability of the proposed APC-based modeling and synchronization framework in richer scattering environments, such as urban canyons, remains to be further validated. In addition, the linear SFO drift assumption adopted in this work is valid for the 40 ms burst considered herein, whereas nonlinear clock drift may become significant under highly dynamic conditions involving rapid maneuvers or severe vibration. Addressing these issues will be an important direction for future work to further improve the generality, robustness, and practical applicability of the proposed framework.

References

[1] Y. Zeng, R. Zhang, and T. J. Lim, “Wireless communications with unmanned aerial vehicles: opportunities and challenges,” *IEEE Commun. Mag.*, vol. 54, no. 5, pp. 36–42, 2016.

[2] M. Mozaffari, W. Saad, M. Bennis, Y.-H. Nam, and M. Debbah, “A tutorial on UAVs for wireless networks: Applications, challenges, and open problems,” *IEEE Commun. Surveys Tuts.*, vol. 21, no. 3, pp. 2334–2360, 2019.

[3] J. Liu, Y. Shi, Z. M. Fadlullah, and N. Kato, “Space-air-ground integrated network: A survey,” *IEEE Commun. Surveys Tuts.*, vol. 20, no. 4, pp. 2714–2741, 2018.

[4] G. Matz, “On non-WSSUS wireless fading channels,” *IEEE Trans. Wireless Commun.*, vol. 4, no. 5, pp. 2465–2478, 2005.

[5] L. Bernadó, T. Zemen, F. Tufvesson, A. F. Molisch, and C. F. Mecklenbräuker, “The (in-) validity of the WSSUS assumption in vehicular radio channels,” in *Proc. IEEE 23rd Int. Symp. Pers., Indoor Mobile Radio Commun. (PIMRC)*, 2012, pp. 1757–1762.

[6] B. Hua *et al.*, “Ultra-wideband nonstationary channel modeling for UAV-to-ground communications,” *IEEE Trans. Wireless Commun.*, vol. 24, no. 5, pp. 4190–4204, 2025.

[7] H. Chang *et al.*, “A novel nonstationary 6G UAV-to-ground wireless channel model with 3-D arbitrary trajectory changes,” *IEEE Internet Things J.*, vol. 8, no. 12, pp. 9865–9877, 2021.

[8] J. Bian, C.-X. Wang, Y. Liu, J. Tian, J. Qiao, and X. Zheng, “3D non-stationary wideband UAV-to-ground MIMO channel models based on aeronautic random mobility model,” *IEEE Trans. Veh. Technol.*, vol. 70, no. 11, pp. 11 154–11 168, 2021.

[9] H. Chang, J. Bian, C.-X. Wang, Z. Bai, W. Zhou, and E.-H. M. Aggoune, “A 3D non-stationary wideband GBSM for low-altitude UAV-to-ground V2V MIMO channels,” *IEEE Access*, vol. 7, pp. 70 719–70 732, 2019.

[10] L. Bai, Z. Huang, T. Feng, and X. Cheng, “A non-stationary channel model for 6G multi-UAV cooperative communication,” *IEEE Trans. Wireless Commun.*, vol. 23, no. 2, pp. 949–961, 2024.

[11] Z. Ma, B. Ai, R. He, G. Wang, Y. Niu, and Z. Zhong, “A wideband non-stationary air-to-air channel model for UAV communications,” *IEEE Trans. Veh. Technol.*, vol. 69, no. 2, pp. 1214–1226, 2020.

[12] A. Colpaert, Z. Cui, E. Vinogradov, and S. Pollin, “3D non-stationary channel measurement and analysis for MaMIMO-UAV communications,” *IEEE Trans. Veh. Technol.*, vol. 73, no. 5, pp. 6061–6072, 2024.

[13] L. Hou, F. Yan, H. Li, K. Ding, W. Xia, and L. Shen, “Non-stationary low-altitude UAV MIMO A2G channel model with rotation and arbitrary trajectories,” *IEEE Trans. Network Sci. Eng.*, vol. 11, no. 2, pp. 1834–1845, 2024.

[14] Z. Ma *et al.*, “Impact of UAV rotation on MIMO channel characterization for air-to-ground communication systems,” *IEEE Trans. Veh. Technol.*, vol. 69, no. 11, pp. 12 418–12 431, 2020.

[15] X. Yang, D. Zhai, R. Zhang, L. Liu, F. R. Yu, and V. C. M. Leung, “Temporal correlation characteristics of air-to-ground wireless channel with UAV wobble,” *IEEE Trans. Intell. Transp. Syst.*, vol. 24, no. 10, pp. 10 702–10 715, 2023.

[16] S. Yang, Z. Zhang, J. Zhang, and J. Zhang, “Impact of rotary-wing UAV wobbling on millimeter-wave air-to-ground wireless channel,” *IEEE Trans. Veh. Technol.*, vol. 71, no. 9, pp. 9174–9185, 2022.

[17] M. Banagar and H. S. Dhillon, “Fundamentals of wobbling and hardware impairments-aware air-to-ground channel model,” *IEEE Trans. Veh. Technol.*, vol. 73, no. 12, pp. 17 946–17 962, 2024.

[18] B. Hua *et al.*, “AAV air-to-air channel: Statistical properties and experimental verification,” *IEEE Internet Things J.*, vol. 12, no. 13, pp. 25 790–25 803, 2025.

[19] X. Wu *et al.*, “60-GHz millimeter-wave channel measurements and modeling for indoor office environments,” *IEEE Trans. Antennas Propag.*, vol. 65, no. 4, pp. 1912–1924, 2017.

[20] D. W. Matolak and R. Sun, “Air–ground channel characterization for unmanned aircraft systems—Part I: Methods, measurements, and models for over-water settings,” *IEEE Trans. Veh. Technol.*, vol. 66, no. 1, pp. 26–44, 2017.

[21] R. Sun and D. W. Matolak, “Air–ground channel characterization for unmanned aircraft systems Part II: Hilly and mountainous settings,” *IEEE Trans. Veh. Technol.*, vol. 66, no. 3, pp. 1913–1925, 2017.

[22] Ó. Seijo, I. Val, and J. A. López-Fernández, “Portable full channel sounder for industrial wireless applications with mobility by using sub-nanosecond wireless time synchronization,” *IEEE Access*, vol. 8, pp. 175 576–175 588, 2020.

[23] X. Cai *et al.*, “An empirical air-to-ground channel model based on passive measurements in LTE,” *IEEE Trans. Veh. Technol.*, vol. 68, no. 2, pp. 1140–1154, 2019.

[24] J. Rodríguez-Piñeiro, T. Domínguez-Bolaño, X. Cai, Z. Huang, and X. Yin, “Air-to-ground channel characterization for low-height UAVs in realistic network deployments,” *IEEE Trans. Antennas Propag.*, vol. 69, no. 2, pp. 992–1006, 2021.

[25] K. Mao *et al.*, “A UAV-aided real-time channel sounder for highly dynamic nonstationary A2G scenarios,” *IEEE Trans. Instrum. Meas.*, vol. 72, pp. 1–15, 2023.

[26] K. Zhang *et al.*, “A three-dimensional time-varying channel model for THz UAV-based dual-mobility channels,” *Entropy*, vol. 26, no. 11, p. 924, 2024.

[27] A. Boriskin and R. Sauleau, Eds., *Aperture Antennas for Millimeter and Sub-Millimeter Wave Applications*. Cham, Switzerland: Springer, 2018.

[28] F. Burmeister, R. Jacob, A. Traßl, N. Schwarzenberg, and G. Fettweis, “Dealing with fractional sampling time offsets for unsynchronized mobile channel measurements,” *IEEE Wireless Commun. Lett.*, vol. 10, no. 12, pp. 2781–2785, 2021.

[29] L. A. López-Valcárcel and M. G. Sánchez, “Characterization, analysis, and modeling of the non-stationary V2I channel at 28-GHz on highways,” *IEEE Trans. Intell. Transp. Syst.*, vol. 26, no. 5, pp. 5961–5974, 2025.

[30] R. He *et al.*, “Characterization of quasi-stationarity regions for vehicle-to-vehicle radio channels,” *IEEE Trans. Antennas Propag.*, vol. 63, no. 5, pp. 2237–2251, 2015.

[31] F. A. Rodríguez-Corbo, L. Azpilicueta, M. Celaya-Echarri, R. Shubair, and F. Falcone, “mmWave channel stationarity analysis of V2X communications in an urban environment,” *IEEE Antennas Wirel. Propag. Lett.*, vol. 22, no. 6, pp. 1406–1410, 2023.

[32] J. H. Bae, Y. S. Kim, N. Hur, and H. M. Kim, “Study on air-to-ground multipath channel and mobility influences in UAV-based broadcasting,” in *Proc. Int. Conf. Inf. Commun. Technol. Converg. (ICTC)*, 2018, pp. 1534–1538.

[33] D. W. Matolak and R. Sun, “Air–ground channel characterization for unmanned aircraft systems—Part III: The suburban and near-urban environments,” *IEEE Trans. Veh. Technol.*, vol. 66, no. 8, pp. 6607–6618, 2017.

[34] H. Chang, J. Bian, C.-X. Wang, Z. Bai, J. Sun, and X. Gao, “A 3D wideband geometry-based stochastic model for UAV air-to-ground channels,” in *Proc. IEEE Global Commun. Conf. (GLOBECOM)*, 2018, pp. 206–212.